Numerical Study of Flexible Flapping Wing Propulsion

Tao Yang[*] and Mingjun Wei[†]

New Mexico State University, Las Cruces, New Mexico 88003

and

Hong Zhao[‡]

University of Illinois at Urbana–Champaign, Urbana, Illinois 61801

In this study, a strong-coupling approach is applied to simulate highly flexible flapping wings interacting with fluid flows. Here, the fluid motion, solid motion, and their interaction are solved together by a single set of equations of motion on a fixed Eulerian mesh, with the elastic stress being solved on a Lagrangian mesh and projected back to the Eulerian mesh. To provide necessary flapping mechanism, control cells are implemented in solid area (i.e., the wing) as "skeleton." The moving trajectory of the skeleton is therefore prescribed by a conventional direct-forcing type of immersed boundary method, while the rest of the wing moves passively through elasticity and fluid–structure interaction. This combined algorithm is then used to study the propulsion characteristics of flexible flapping wings with different elastic moduli and at different flapping frequencies and amplitudes. A two-dimensional NACA0012 airfoil is chosen as a model wing, and it is under active plunging defined by control cells and corresponding passive pitching motion. With different input parameters, very different wake structures can be observed. As a result, the coupled plunging-pitching motion can be either drag-producing or thrust-producing. Finally, passive pitching angle θ and nominal angle of attack α for flexible wings are defined to characterize the flapping motion. It is found that θ needs to be greater than 0.26 and α needs to be greater than 0.3 to generate thrust instead of drag for the flapping motion within the current parametric matrix.

Nomenclature

$\mathbf{A}$	=	solid deformation gradient tensor, $\partial \mathbf{x}/\partial \mathbf{X}$
a	=	amplitude of the oscillatory motion
$\mathbf{B}$	=	body force to present solid effects in body area
c	=	initial chord length of the foil (before deformation)
$\mathbf{F}$	=	surface force to present solid effects at fluid-solid interface
k	=	frequency of the oscillatory motion, $k^* c^*/U^*$
p	=	pressure
Re	=	Reynolds number, $\rho^* U^* c^*/\mu_f^*$
U	=	incoming flow velocity
$\mathbf{u}$	=	velocity vector in a Eulerian mesh for both fluid and solid, (u, v)
$\mathbf{V}$	=	velocity of control cells
v_x and v_y	=	nondimensional velocity along x and y directions respectively
$\mathbf{X}$	=	coordinate of a solid material point at a reference state
$\mathbf{x}$	=	current coordinate of a solid material point
x and y	=	nondimensional coordinate system, x is defined along U^*

Greek Symbols

α	=	nominal angle of attack
Δt	=	time-step size
θ	=	passive pitching angel
μ_f	=	dynamic viscosity for fluid
μ_s	=	solid shear modulus
μ_{fs}	=	nominal dynamic viscosity for solid
ρ	=	density
τ	=	stress tensor
τ_{elas}	=	elastic part of the stress tensor for solid
τ_{visc}	=	viscous part of the stress tensor for solid
Ω_c	=	control-cell area
Ω_s	=	solid (wing) area

Subscripts

f	=	properties for fluid
s	=	properties for solid
max	=	instantaneous maximum value for θ and α

Superscript

$*$	=	dimensional properties

*Ph.D. Candidate, Department of Mechanical and Aerospace Engineering. Student Member AIAA.

†Assistant Professor, Department of Mechanical and Aerospace Engineering. Senior Member AIAA.

‡Currently Research Associate, Stanford University, Palo Alto, CA.

I. Introduction

THE fact that birds and insects use flapping wings to generate lift and thrust has inspired the earliest idea for mechanical flight in human history. However, the human-carrying flight has been dominated by the fixed-wing design for its simplicity. Recently, with the demand for micro air vehicles, there is renewed interest in the flapping wing design. At low Reynolds number, conventional fixed-wing airplanes suffer with low flight efficiency and small stall angle. The flapping motion can increase the effective Reynolds number seen by the wing. At the same time, the flapping wing design offers other desirable characteristics in maneuverability, flutter, and energy efficiency [1].

The thrust generated by a flapping wing was firstly and independently observed by Knoller in 1909 [2] and Betz in 1912 [3]. The Knoller-Betz effect was verified experimentally in a wind tunnel by Katzmayr in 1922 [4]. In 1935, based on an observation of the location and orientation of vortex pairs in the wake, von Kármán and Burgers [5] gave a theoretical explanation for the drag and thrust production by flapping wings. Applying Theodorsen's inviscid,

incompressible, oscillatory flat-plate theory, Garrick [6] concluded that plunging foils generate thrust all the time and pitching foils generate thrust only with high enough frequencies. Since then, many studies were done to understand the flapping motion, or more precisely, plunging motion, pitching motion, and their combination. More complete history of early research in the field has been covered in various places [7–10]. The majority of early works focused on rigid two-dimensional airfoils, and early numerical simulations were mostly for inviscid flow [7]. The inviscid assumption, however, made large discrepancy with experiments at low oscillatory frequency. Another factor normally ignored in early studies is airfoil flexibility. Although people have noticed the advantages (e.g. aerodynamic efficiency, design simplification) of introducing flexibility in flapping wings, the study for flexible wings was hindered by its complexity. Recently, Heathcote and Gursul [10] did an interesting experiment in their water channel to study the thrust efficiency with different flexibility, oscillation frequency, and shape characteristics. The active motion was plunging only, and the pitching motion was introduced passively by the flexibility. For rigid wings, Anderson et al. [11] have concluded that there is an optimal phase angle between the pitching and plunging for thrust efficiency. Heathcote and Gursul [10] made a similar effort for the optimal phase angel between active plunging and passive pitching for flexible foils in their experiment. On numerical simulation side, the difficulty to include the flexibility lies in efficiently computing the fully-coupled motion between the fluid and structure, especially when large nonlinear deformation presents. Instead of truly flexible body, deformable body with prescribed motion and deformation was often studied as a substitution, and provided some interesting insight [12].

Another interesting result is deflected wake vortex streets, which have been observed both experimentally and numerically for plunging rigid wings [7,13]. The inclined direction was observed to depend on initial conditions in most simulations. Lewin and Haj-Hariri also observed the switch of the inclined directions under particular conditions [14]. In this paper, similar wake deflection for flexible wings will be studied.

The purpose of the current work is to numerically investigate the propulsion characteristics by flapping flexible wings with fully-coupled interaction between the wing and surrounding fluid. The paper is arranged to describe the algorithm in Sec. II, conduct case study and discuss the results in Sec. III, and summarize the final conclusion in Sec. IV.

II. Numerical Algorithm

The current simulation algorithm was modified from a strong-coupling approach for fluid–structure interaction (FSI) recently proposed by Zhao et al. [15]. In their work, a uniform set of equations was solved simultaneously for fluid and solid with simple implementation and approximately second-order accuracy. However, the original approach can not be applied directly to flapping wing simulation for its lack of trajectory control mechanism. Therefore, we implemented rigid control cells inside the elastic body as skeleton structure to flap the wing. To assure an accurate description of the skeleton's moving trajectory, a typical immersed boundary method using direct-forcing approach [16] was applied on the control cells only and fitted into the otherwise elastic body moving passively through FSI. In this section, we first give a brief review of the FSI approach by Zhao et al. [15], then describe our implementation of control cells. Other simulation detail is given at the end.

A. Fluid–Structure Interaction in a Strong Form

For the completeness of the paper, the original FSI approach by Zhao et al. [15] is summarized briefly here with some adaptation in notations.

In a Eulerian framework, the mass and momentum conservation for fluid and solid can be presented in the same manner as

$$\nabla^* \cdot \mathbf{u}^* = 0 \qquad (1)$$

$$\frac{\partial \mathbf{u}^*}{\partial t^*} + \mathbf{u}^* \cdot \nabla^* \mathbf{u}^* = -\frac{1}{\rho^*}\nabla^* p^* + \frac{1}{\rho^*}\nabla^* \cdot \tau^* \qquad (2)$$

For Newtonian fluid, the stress tensor

$$\tau_f^* = \mu_f^*(\nabla^* \mathbf{u}^* + \nabla^* \mathbf{u}^{*T}) \qquad (3)$$

The substitution of Eq. (3) into momentum equation leads to the famous Navier–Stokes equation for fluid flow:

$$\frac{D\mathbf{u}^*}{Dt^*} = -\frac{1}{\rho_f^*}\nabla^* p^* + \frac{\mu_f^*}{\rho_f^*}\nabla^{*2}\mathbf{u}^* \qquad (4)$$

For solid, the stress tensor includes both viscous and elastic components:

$$\tau_s^* = \tau_{\text{elas}}^* + \tau_{\text{visc}}^* \qquad (5)$$

where, τ_{visc}^* is assumed to be similar to fluid viscous stress by replacing the coefficient μ_f^* of Eq. (3) with a nominal μ_{fs}^*. The elastic stress term using a neo-Hooken model is

$$\tau_{\text{elas}}^* = \mu_s^*(\mathbf{A} \cdot \mathbf{A}^T - \mathbf{I}) \qquad (6)$$

Thus, the momentum equation for solid is

$$\frac{D\mathbf{u}^*}{Dt^*} = -\frac{1}{\rho_s^*}\nabla^* p^* + \frac{\mu_{fs}^*}{\rho_s^*}\nabla^{*2}\mathbf{u}^* + \frac{1}{\rho_s^*}\nabla^* \cdot \tau_{\text{elas}}^* \qquad (7)$$

Equations (4) and (7) can be unified to a combined momentum equation:

$$\frac{D\mathbf{u}^*}{Dt^*} = -\frac{1}{\rho^*}\nabla^* p^* + \frac{\mu^*}{\rho^*}\nabla^{*2}\mathbf{u}^* + \mathbf{B}^* + \mathbf{F}^* \qquad (8)$$

where ρ^* can be either ρ_f^* or ρ_s^*, μ can be either μ_f^* or μ_{fs}^*, and the extra body force $\mathbf{B}^*$ and surface force $\mathbf{F}^*$ are defined in a confined solid area Ω_s to present the elasticity. If a characteristic function χ_s is introduced as

$$\chi_s = \begin{cases} 1 & \text{in } \Omega_s \\ 0 & \text{otherwise} \end{cases} \qquad (9)$$

we have then

$$\mathbf{B}^* + \mathbf{F}^* = \nabla^* \cdot (\chi_s \tau_{\text{elas}}^*) \qquad (10)$$

Two assumptions were made in Zhao et al.'s work [15]: 1) $\rho_s^* = \rho_f^*$; 2) $\mu_{fs}^* = \mu_f^*$. These assumptions are also adopted here. Therefore, inertial effects to propulsion and detail modeling for solid viscosity are excluded from our current study.

We then use ρ_f^*, μ_f^*, U^*, and c^* to nondimensionalize Eq. (8) to

$$\frac{\partial \mathbf{u}}{\partial t} + \mathbf{u} \cdot \nabla \mathbf{u} = -\nabla p + \frac{1}{Re_f}\nabla^2 u + \nabla \cdot (\chi_s \tau_{\text{elas}}) \qquad (11)$$

where

$$Re_f = \frac{\rho_f^* U^* c^*}{\mu_f^*} \qquad \tau_{\text{elas}} = \mu_s(\mathbf{A} \cdot \mathbf{A}^T - \mathbf{I}), \qquad \mu_s = \frac{\mu_s^*}{\rho_s^* U^{*2}}$$

The numerical implementation of Eq. (11) for FSI becomes easy by allowing conventional simulation methods for incompressible Navier–Stokes equations (e.g. projection method [17]). Since elastic stress calculation is sensitive to the location of solid material points, the elastic stress term is computed separately on a Lagrangian mesh. So, information is exchanged constantly between the overall Eulerian mesh and the local (structure) Lagrangian mesh at each time step. The projection/interpolation between the meshes as well as other algorithm details are referred to Zhao et al.'s original work [15].
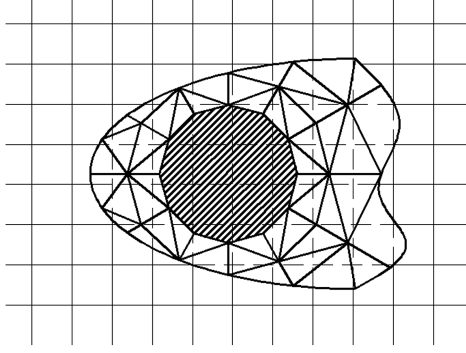
Fig. 1 The sketch of mesh configuration for a NACA airfoil: Cartesian mesh with thin lines is the global Eulerian mesh; triangles with thick lines are the local Lagrangian mesh for solid; control cells are shaded.
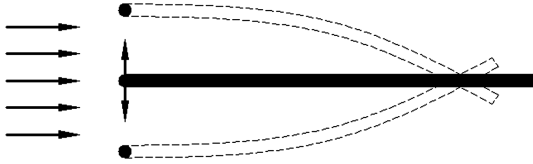

Fig. 2 Schematics for flapping motion.

B. Implementation of Control Cells

The preceding FSI algorithm can solve the coupled dynamics of the fluid and structure. However, it lacks the mechanism to define the motion of certain components (i.e. skeleton) for the desirable moving trajectory (i.e. flapping). To solve this problem, we introduce a few control cells at the leading edge (Fig. 1), and define their moving gaits in a way similar to the direct-forcing approach [16] which has been widely used for prescribed motion. In our study, to mimic a rigid rod, the control cells are in a circular area Ω_c with its center at $0.04c^*$ behind the airfoil front point and on the center line and with the diameter also being $0.04c^*$.

If the momentum equation is discretized in time as

$$\frac{\mathbf{u}^{n+1} - \mathbf{u}^n}{\triangle t} = (\mathrm{RHS})^n \tag{12}$$

where all right-hand-side terms (RHS), including body force and surface force terms for solid, are lumped into the term RHS, a body force term confined in control-cell area Ω_c can be defined by

$$f = \begin{cases} -(\mathrm{RHS})^n + \frac{1}{\triangle t}(\mathbf{V} - \mathbf{u}^n) & \text{in } \Omega_c \\ 0 & \text{otherwise} \end{cases} \tag{13}$$

So that, we can use control-cell velocity $\mathbf{V}$ to define the exact moving trajectory of the leading edge. Then, the final momentum equation with flapping capability is

$$\frac{\partial \mathbf{u}}{\partial t} + \mathbf{u} \cdot \nabla \mathbf{u} = -\nabla p + \frac{1}{Re_f}\nabla^2\mathbf{u} + \nabla \cdot (\chi_s \tau_{\mathrm{elas}}) + \chi_c f \tag{14}$$

where χ_c is defined similarly but with value only in Ω_c. Here, first-order explicit time difference is used only for easy demonstration, and in practice, we use third-order Runge–Kutta/Crank–Nicolson scheme following the same spirit.

C. Simulation Setup

Using this combined approach, we are able to simulate flapping flexible wings with well-controlled leading-edge motion and fully-coupled dynamics.

The computational domain was a square area with $-4 < x < 4$ and $-4 < y < 4$ nondimensionalized by c^*. The mesh size 800×800 was used for most cases, while 1600×1600 was used for the cases with high oscillatory frequencies ($k \geq 3$). Uniform staggered-mesh was used in the discretization of global Eulerian coordinate.

For the Lagrangian mesh used in computing structural stress terms, triangular cells showed better stability than rectangular cells and were picked for all cases studied in this paper. Other constraints for grid generation included: 1) the solid cell size should be about the same as or larger than Cartesian cell [15]; 2) the solid cells should be discretized in a symmetric way if symmetric airfoil is used (i.e. NACA0012).

Figure 2 shows schematically the flapping motion acquired in the computation. The control cells at the leading edge move vertically at speed

$$v_x = 0, \qquad v_y = 2ak\pi\cos(2k\pi t) \tag{15}$$

In our simulation, the Reynolds number was 500, and non-dimensional solid elastic shear modulus is usually $\mu_s = 1000$ (except when we study the elastic effects).

III. Results and Discussions

In this section, we first check the numerical convergency of our method, then numerically study the propulsion characteristics at different flapping frequency, amplitude, and with different wing material (i.e. shear modulus).

A. Algorithm Convergence

Since there was no exact solution, we ran a base case with $a = 0.1$ and $k = 1$ at very fine mesh 3200×3200 and use it as a benchmark to study the convergency from coarser meshes: 200×200, 400×400, 800×800, and 1600×1600. The Lagrangian mesh was changed accordingly. To check the accuracy of the fluid computation, we compared the velocity in a square area downstream (Fig. 3a); to check the accuracy of the solid structure computation, we compared the locations of the solid material points along the center line (Fig. 3b). The accuracy between first- and second-order was shown for both fluid computation (Fig. 4) and solid computation (Fig. 5). It is similar to the order of Zhao et al.'s [15] original FSI algorithm. Thus, the implementation of control cells has not degraded the general FSI algorithm.

The base case has also run for different domain sizes to check the domain independence. It was shown that the current computational domain is adequate in a sense that the error brought in by finite domain size is at the same order of other numerical errors.

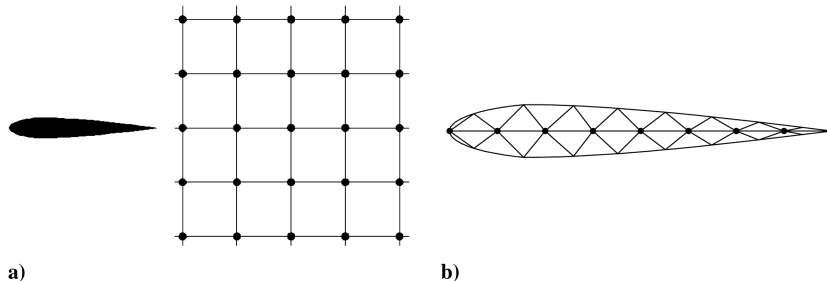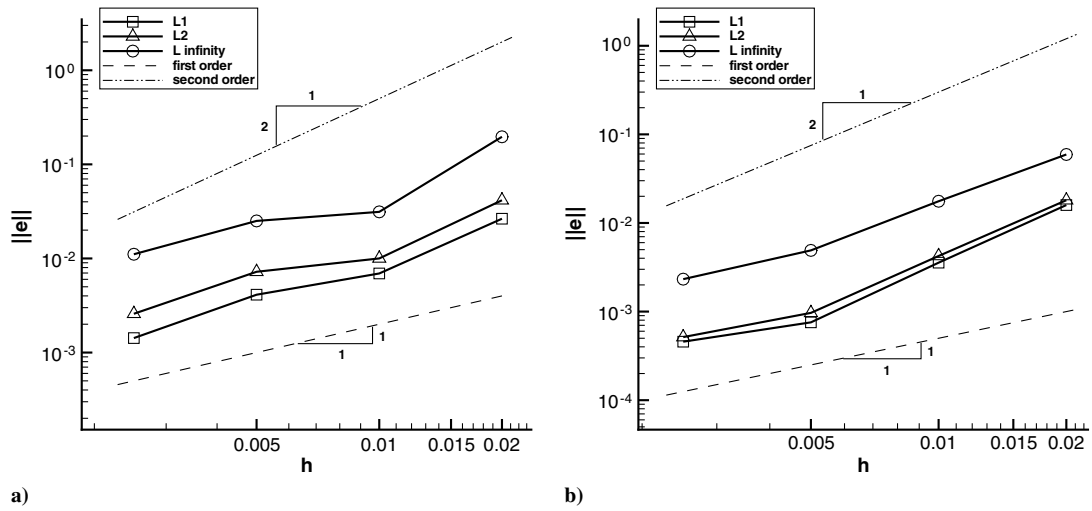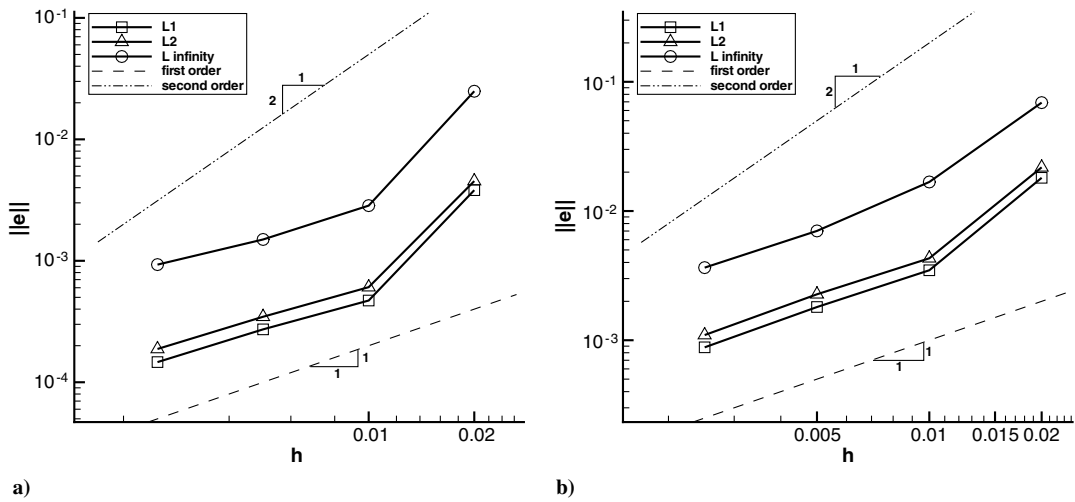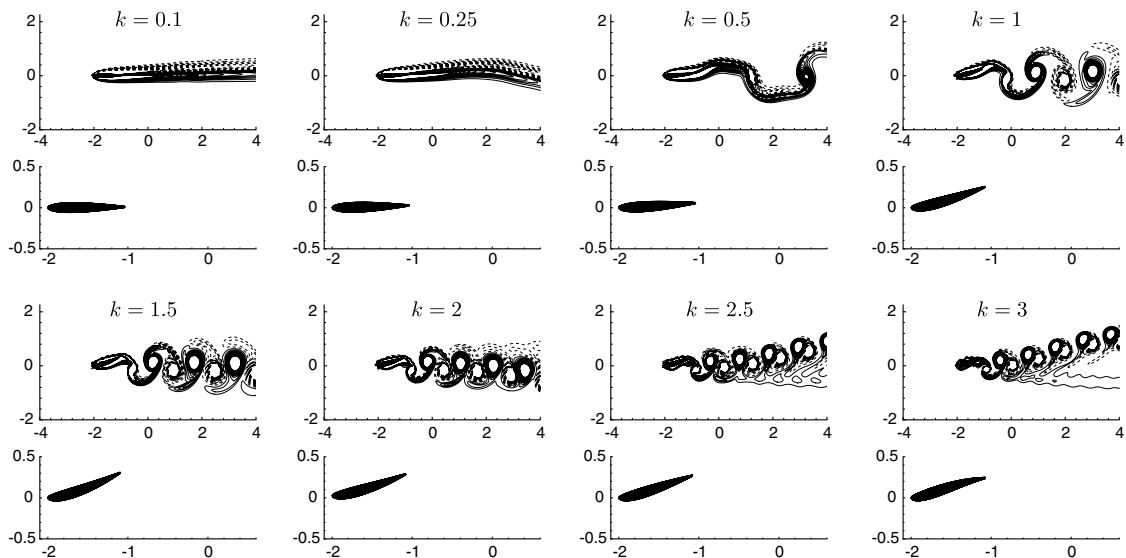a)   b)

Fig. 3 Sketch for points used in convergence study: a) Eulerian points used to compare flow velocity and b) Lagrangian points used to compare structure deformation.

Fig. 4   Error of flow velocity: a) *u* and b) *v*.

Fig. 5   Error of structure deformation: a) along *x* and b) along *y*.

Fig. 6   Wake patterns for the flapping motion with *a* = 0.1 but at different frequencies. The top part shows the flowfield with vorticity contours (—— for positive and ---- for negative values); the bottom part shows the zoom-in detail of wing deformation (the same will be for similar figures later without explanation).
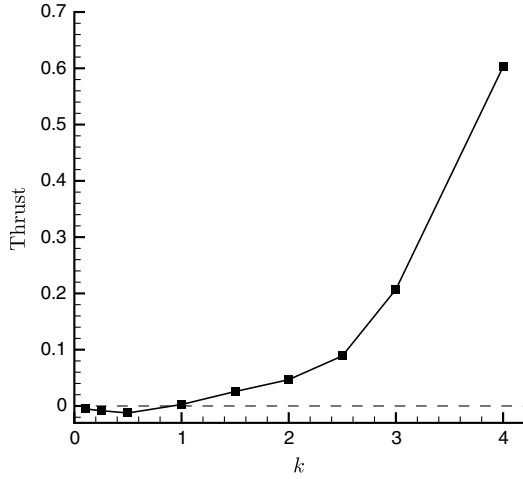
Fig. 7   The thrust/drag produced by the flapping motion with $a = 0.1$ but at different frequencies.
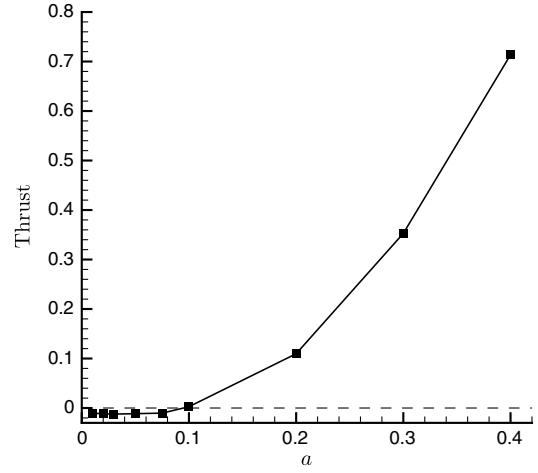

Fig. 9   The thrust/drag produced by the flapping motion at $k = 1$ but with different amplitudes.

B.   Propulsion Characteristics

Three design parameters are studied in this paper for their effects to propulsion efficiency: 1) flapping frequency: for $a = 0.1$, the control cells plunge at different frequencies $k = 0.1$, 0.25, 1, 1.5, 2, 2.5, 3, and 4; 2) flapping amplitude: for $k = 1$, the oscillatory amplitude of the control cells are $a = 0.01$, 0.02, 0.03, 0.05, 0.075, 0.1, 0.2, 0.3, and 0.4; and 3) shear modulus: for the same $a = 0.1$ and $k = 1$, we pick different shear moduli $\mu_s = 10$, 100, 200, 500, 1000, 1250, 1500, and 2000.

1.   Effects of Flapping Frequency

Figure 6 shows different wake patterns as the frequency increases while the amplitude a stays at 0.1. As the frequency increases, the vortex starts to shed; then, it immediately appears as a reverse Kármán vortex street without the transition from a Kármán vortex street; eventually, the deflected vortex street appears at higher frequencies in a similar fashion observed for rigid wings in pure plunging motion [7,13,14]. In our numerical study, the inclined direction of deflected vortex streets is solely determined by the initial conditions.

By measuring the mean velocity profile at downstream location ($x = 2$ for our case), one can estimate the thrust/drag by a simple control-volume calculation [11]. Figure 7 shows the relation between the frequency and the thrust. There is actually small drag when the

wing flapping at very low frequency. We believe that the drag is mainly caused by viscosity instead of vortex induction, because there is no Kármán vortex street observed for the cases at $a = 0.1$. At higher frequencies, the thrust is generated, and it is clearly due to the induced velocity by vortex pairs.

2.   Effects of Flapping Amplitude

Similar study has been done to check the amplitude effects for the flapping motion at the same frequency $k = 1$. Figure 8 shows different wake patterns at different flapping amplitudes. Here, the vortex shedding starts from the very beginning when $a = 0.01$, and a Kármán vortex street is clearly observed; later, the wake structure is changed to a reverse Kármán vortex street; finally, when the amplitude is high enough, the vortex shedding shows complex 2p pattern [18], which has not been observed in any low-amplitude cases in current study. Shown in Fig. 9, at low frequency, there is drag produced by both viscosity and the Kármán vortex street; when frequency increases, the clear thrust is produced by the reverse Kármán vortex street and the complex 2p vortex shedding later.

3.   Effects of Shear Modulus

The effects of the shear modulus of wing material are studied for the case flapping at $a = 0.1$ and $k = 1$. Figure 10 shows different wake patterns for different shear moduli.
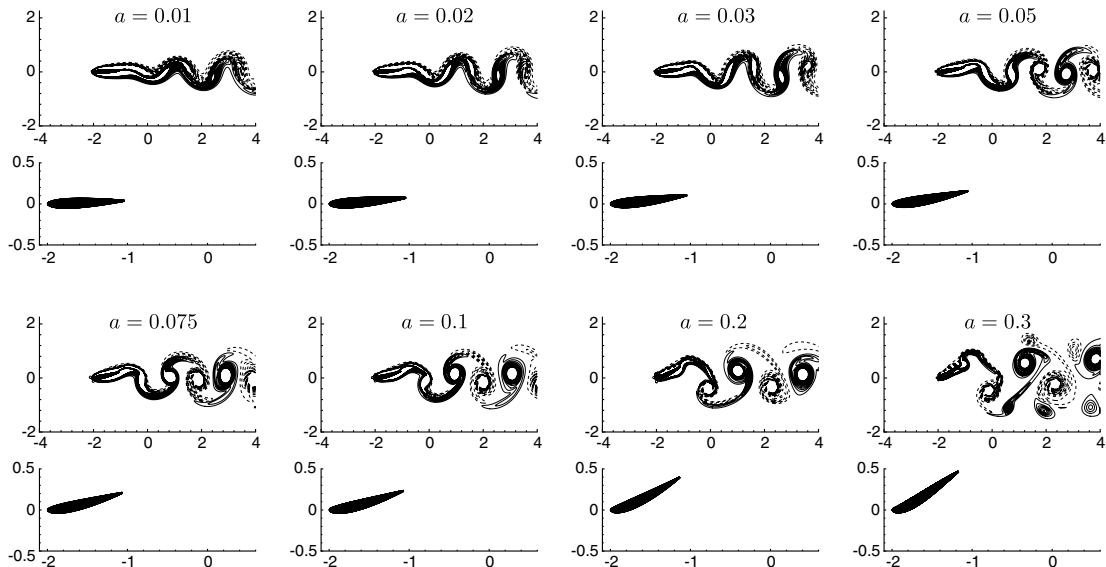

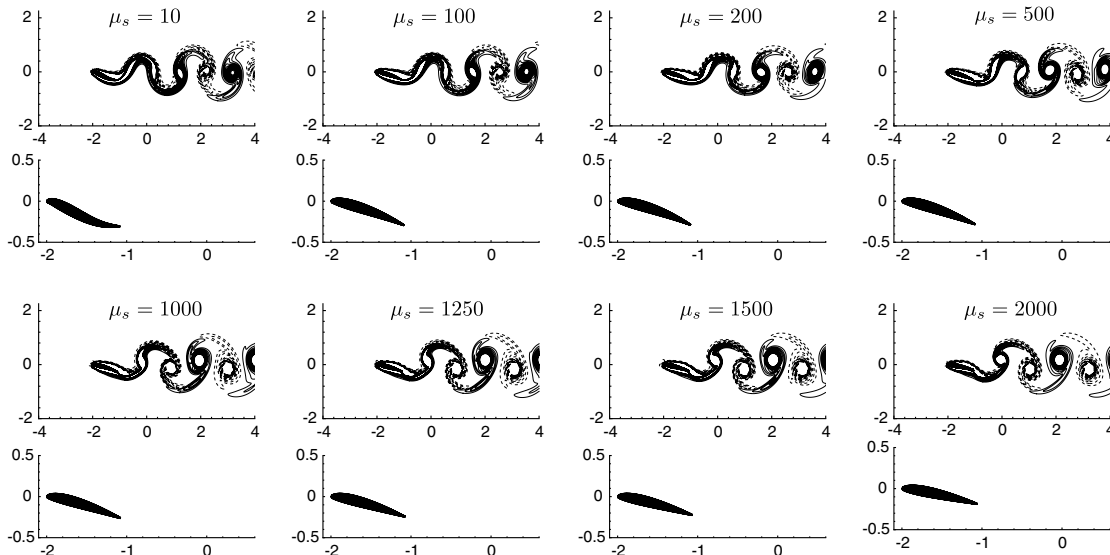**Fig. 8   Wake patterns for the flapping motion at $k = 1$ but with different amplitudes.**

Fig. 10 Wake patterns for wings with different shear moduli and all flapping at $a = 0.1$ and $k = 1$.

While shear modulus increases, the wake vortex structure changes from the Kármán vortex street to the reverse Kármán vortex street. This transition makes the change for the flapping motion from drag-producing to thrust-producing, which is shown more clearly in the thrust/drag calculation in Fig. 11. The changes for vortex structure and thrust are less sensitive to shear modulus than other two factors, though the shear modulus still plays an important role and can easily alter the system between drag-producing and thrust-producing as shown.
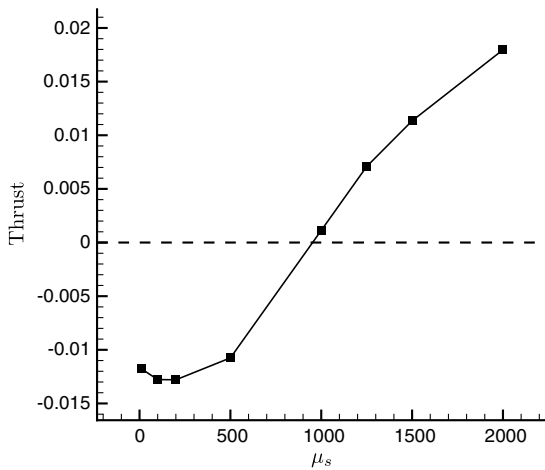

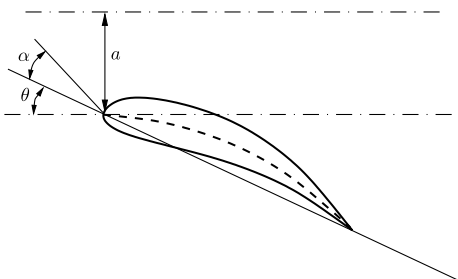**Fig. 11 The thrust/drag produced by flapping at $k = 1$, $a = 0.1$ for airfoils with different shear moduli.**

Fig. 12 Definition of passive pitching angle θ and nominal angle of attack α.

4. Relation to Passive Pitching Angle and Nominal Angle of Attack

As a flexible wing undergoing active plunging, passive pitching is naturally induced. The characteristics of the passive pitching motion are more complex for flexible body, and they are determined by many factors including those discussed before: frequency, amplitude, and shear modulus. Simple observation from the preceding results shows certain correlation between the pitching angle and the wake pattern. In our case, pitching is essentially the result of structure bending. So, in Fig. 12, we define pitching angle θ in a way similar to the one used by Heathcote and Gursul in their experiments about flexible wings [10]. In Anderson et al.'s experiments of rigid airfoils with a combined motion of active plunging and active pitching, they suggested a nominal angle of attack to characterize the flapping motion [11]. Similarly, for flexible foils, we can also define a nominal angle of attack by

$$\alpha = \arctan\left(\frac{2ak\pi}{U}\right) - \theta \qquad (16)$$

as shown in Fig. 12.

It is noticed that this definition of nominal angle of attack is accurate only when the phase angle between the plunging and the pitching motion is exactly $90°$. This condition is approximately met in all our cases. There are various ways (e.g. increasing flapping
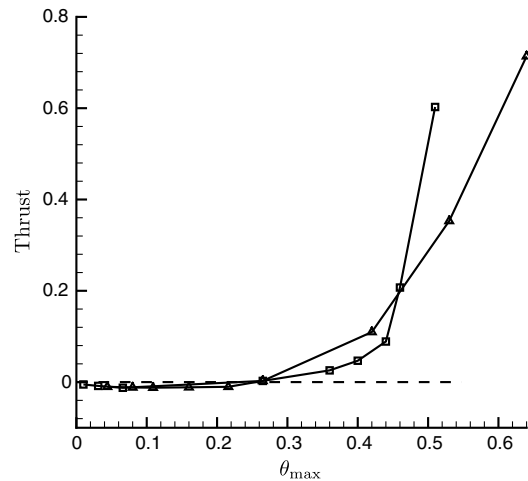

Fig. 13 The relationship between the thrust and the maximum pitching angle $\theta_{\max}$. $\square$: with k being changed and a fixed; $\triangle$: with a being changed and k fixed.
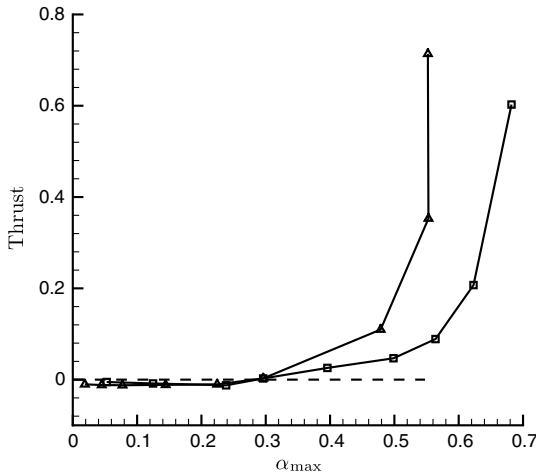
Fig. 14   The relationship between the thrust and the maximum nominal angle of attack α_{max}. $\square$: with k being changed and a fixed; $\triangle$: with a being changed and k fixed.

frequency or amplitude) capable of increasing the maximum θ and α. Though the angles are changed by different reasons (i.e. frequency or amplitude), Figs. 13 and 14 plot a direct relation between these two angles and the generated thrust. Despite different driven factors, for both θ and α, threshold values ($\theta \approx 0.26$, $\alpha \approx 0.3$ in our cases) are indicated for the flapping motion to change from the drag-producing to the thrust-producing. This critical point seems to be associated with the moment when a reverse Kármán vortex street appears. The thrust force keeps increasing as θ and α both increase. However, in both Figs. 13 and 14, it is also shown that the line driven by increasing the frequency and and the one driven by increasing the amplitude start to depart from each other after some point. This can be explained by their very different vortex structures in the frequency-driven and the amplitude-driven cases at large θ and α. Higher frequency produces the deflected vortex street, and higher amplitude changes the vortex structure from 2s pairing to 2p pairing instead. For such cases, one single parameter along, either θ or α, can not explain the whole complex vortex dynamics any more, though these angles still play critical roles.

IV.   Conclusions

We have successfully developed a combined algorithm to study flapping flexible wings under active plunging and passive pitching motion. The overall continuity equation and momentum equations were solved in a uniform Eulerian coordinate, while the solid elasticity and the moving trajectory of control cells are both presented by body force terms defined in a Lagrangian solid region and a Lagrangian control-cell region, respectively. The implementation of control cells has not degraded the original accuracy of Zhao et al.'s [15] FSI algorithm.

The propulsion effects of flapping frequency and amplitude and solid shear moduli were then studied using this combined algorithm.

The structure of wake vortex street and the mean velocity profile at downstream location both indicate that the flexible wings generate thrust when they flapping at high frequency and large amplitude and generate drag at low frequency and small amplitude. As the frequency and amplitude keep increasing, the thrust force also increases. At high frequency, the vortex street will eventually deflect upward or downward, and at large amplitude, more complex vortex structure with 2p pairing occurs. As material shear modulus increases, we can also observe that the wake vortex changes from drag-producing to thrust-producing.

The preceding parametric study shows a correlation between propulsion characteristics and structure bending, which can be quantified approximately by a passive pitching angle θ induced by active plunging motion. Nominal angle of attack α for flexible wings can therefore be defined and also used to characterize the flow. Both θ

and α show threshold values for the flapping motion to change from the drag-producing to the thrust-producing. However, more complex wake structure, such as 2p vortex pairing or deflected vortex street, are not expected to be explained by any single parameter alone.

References

[1] Mueller, T. J., and DeLaurier, J. D., "An Overview of Micro Air Vehicle Aerodynamics," *Fixed and Flapping Wing Aerodynamics for Micro Air Vehicle Applications*, edited by T. J. Mueller, AIAA, Reston, VA, 2001.

[2] Knoller, R., "Die Gesetze des Luftwiderstandes," *Flug- und Motortechnik (Wien)*, Vol. 3, No. 21, 1909, pp. 1–7.

[3] Betz, A., "Ein Beitrag zur Erklärung des Segelfluges," *Zeitschrift für Flugtechnik und Motorluftschiffahrt*, Vol. 3, Jan. 1912, pp. 269–272.

[4] Katzmayr, R., "Effect of Periodic Changes of Angle of Attack on Behavior of Airfoils," NACA Rept. 147, Oct. 1922 (translated from "Zeitschrift fur Flugtechnik und Motorluftschiffahrt," 31 March 1922, pp. 80–82, and April 13, 1922, pp. 95–101).

[5] von Kármán, T., and Burgers, J. M., *General Aerodynamics Theory: Perfect Fluids*, Julius–Springer, Berlin, 1943.

[6] Garrick, I. E., "Propulsion of a Flapping and Oscillating Airfoil," NACA Rept. 567, 1936.

[7] Jones, K. D., Dohring, C. M., and Platzer, M. F., "Experimental and Computational Investigation of the Knoller–Betz Effect," *AIAA Journal*, Vol. 36, No. 7, 1998, pp. 1240–1246.
doi:10.2514/2.505

[8] Jones, K. D., and Platzer, M. F., "An Experimental and Numerical Investigation of Flapping Wing Propulsion," 37th Aerospace Sciences Meeting, AIAA Paper 99-0995, Reno, NV, Jan. 1999.

[9] Jones, K. D., and Platzer, M. F., "Flapping-Wing Propulsion for a Micro Air Vehicle," 38th Aerospace Sciences Meeting, AIAA Paper 2000-0897, Reno, NV, Jan. 2000.

[10] Heathcote, S., and Gursul, I., "Flexible Flapping Airfoil Propulsion at Low Reynolds Numbers," *AIAA Journal*, Vol. 45, No. 5, 2007, pp. 1066–1079.
doi:10.2514/1.25431

[11] Anderson, J. M., Streitlien, K., Barrett, D. S., and Triantafyllou, M. S., "Oscillating Foils of High Propulsive Efficiency," *Journal of Fluid Mechanics*, Vol. 360, 1998, pp. 41–72.
doi:10.1017/S0022112097008392

[12] Miao, J. M., and Ho, M. H., "Effect of Flexure on Aerodynamic Propulsive Efficiency of Flapping Flexible Airfoil," *Journal of Fluids and Structures*, Vol. 22, 2006, pp. 401–419.
doi:10.1016/j.jfluidstructs.2005.11.004

[13] Lai, J. C. S., and Platzer, M. F., "Jet Characteristics of a Plunging Airfoil," *AIAA Journal*, Vol. 37, No. 12, 1999, pp. 1529–1537.
doi:10.2514/2.641

[14] Lewin, G. C., and Haj-Hariri, H., "Modelling Thrust Generation of a Two-Dimensional Heaving Airfoil in a Viscous Flow," *Journal of Fluid Mechanics*, Vol. 492, 2003, pp. 339–362.
doi:10.1017/S0022112003005743

[15] Zhao, H., Freund, J. B., and Moser, R. D., "A Fixed-Mesh Method for Incompressible Flow-Structure Systems with Finite Solid Deformations," *Journal of Computational Physics*, Vol. 227, 2008, pp. 3114–3140.
doi:10.1016/j.jcp.2007.11.019

[16] Mohd-Yusof, J., "Combined Immersed-Boundary/B-Spline Methods for Simulations of Flow in Complex Geometries," Center for Turbulence Research, Annual Research Briefs, 1997, pp. 317–328.

[17] Brown, D. L., Cortez, R., and Minion, M. L., "Accurate Projection Methods for the Incompressible Navier–Stokes Equations," *Journal of Computational Physics*, Vol. 168, 2001, pp. 464–499.
doi:10.1006/jcph.2001.6715

[18] Williamson, C. H. K., and Roshko, A., "Vortex Formation in the Wake of an Oscillating Cylinder," *Journal of Fluids and Structures*, Vol. 2, 1988, pp. 355–381.
doi:10.1016/S0889-9746(88)90058-8

X. Zhong
Associate Editor